

## Hydrothermal Synthesis

# Sodium Transition Metal Vanadates from Hydrothermal Brines: Synthesis and Characterization of $\text{NaMn}_4(\text{VO}_4)_3$ , $\text{Na}_2\text{Mn}_3(\text{VO}_4)_3$ , and $\text{Na}_2\text{Co}_3(\text{VO}_4)_2(\text{OH})_2$

Tiffany M. Smith Pellizzeri,<sup>[a,b]</sup> Gregory Morrison,<sup>[c]</sup> Colin D. McMillen,<sup>[a]</sup> Hans-Conrad zur Loyer,<sup>[c]</sup> and Joseph W. Kolis<sup>\*[a,d]</sup>

**Abstract:** Three new examples of transition metal vanadates have all been synthesized by a related hydrothermal synthetic route using variations of sodium hydroxide/sodium chloride brines as mineralizers. Compound **1**,  $\text{NaMn}_4(\text{VO}_4)_3$ , is built from equivalent interlocking chains of  $\text{Mn}^{2+}$  edge shared octahedra, further coordinated to one another by  $(\text{VO}_4)^{3-}$  vanadate groups to form a three-dimensional structure. Compound **2**,  $\text{Na}_2\text{Mn}_3(\text{VO}_4)_3$ , forms a complex three-dimensional structure of mixed-valence  $2+/3+$  manganese edge-sharing octahedra forming chains, with  $(\text{VO}_4)^{3-}$  tetrahedra acting as space-filters in the structure. Structure **3**,  $\text{Na}_2\text{Co}_3(\text{VO}_4)_2(\text{OH})_2$ , is built of a two-dimensional distorted honeycomb of edge shared  $\text{Co}^{2+}$  lay-

ers decorated by, but not connected by, vanadate groups. The layers bear a relationship to Kagome nets but the structure contains no ideal trigonal symmetry. All compounds were characterized by single-crystal X-ray diffraction. Compounds **1** and **3** were characterized by magnetic susceptibility. The magnetic susceptibility of **1** displays the moment characteristic of  $\text{Mn}^{2+}$  and a transition at 46 K to a spin canted antiferromagnet. Compound **3** shows evidence of spin-orbit coupling in the  $\text{Co}^{2+}$  ions with antiferromagnetic ordering at 4.4 K and highly anisotropic field-dependent behavior with multiple metamagnetic transitions.

## 1. Introduction

Vanadates are versatile and useful oxyanion building blocks for the exploratory synthesis of new transition metal compounds because of their adaptability to different oxidation states and coordination geometries within a structure.<sup>[1–6]</sup> Generally, as a tetrahedral unit, vanadate oxyanions are observed in the +5 oxidation state,  $(\text{VO}_4)^{3-}$ , and therefore have a magnetically inactive  $d^0$  electronic configuration. These building blocks can exist as isolated tetrahedra, or they can coordinate into a wide array of corner-sharing polyvanadates. These vanadate oxyanions can coordinate magnetically active first-row transition metals (i.e.  $\text{Mn}^{2+/3+}$ ,  $\text{Co}^{2+}$ ,  $\text{Fe}^{2+/3+}$ ) to generate a rich assortment of structurally diverse and magnetically interesting compounds.<sup>[7–12]</sup> These materials are generally synthesized at relatively high tem-

peratures using traditional solid-state techniques, such as melts or fluxes.<sup>[5,13–15]</sup> Alternatively, our group found that high temperature (500–700 °C) hydrothermal synthesis leads to a wide range of unusual new transition metal vanadates, often in the form of large, high-quality single crystals.<sup>[9,16–19]</sup> In addition to their new structure types, many of these materials have interesting magnetic properties.

Recently, our group has been extending this concept to the use of hydrothermal brines as solvents to synthesize new transition metal containing compounds. Our successful earlier work with first-row transition metal vanadates encouraged us to employ them as a prototype testbed as we extend our investigation using hydrothermal brines as reaction media. Brines are interesting for several reasons. They often emulate natural geothermal systems and hence can provide clues to mineralogical reaction pathways. The brine components can sometimes act both as mineralizer and a synthetic component, and we have observed that both the cations and anions of the brines have found their way into the lattice of the final products in various reactions. Finally, it is obvious that the chemistry of these fluids and the ultimate final products are highly sensitive to the composition of the brines and these formulations provide yet another chemical knob to adjust, leading to an almost infinite array of new solids. Thus far, we investigated vanadate synthesis from hydrothermal brines based on the hydroxides, carbonates, fluorides, and chlorides of cesium, barium, and strontium.<sup>[7,16–18,20–25]</sup> We now extend our study to the use of mixed sodium chloride/sodium hydroxide brines as the mineralizer in reactions with transition metals and vanadate building

[a] Dr. T. M. Smith Pellizzeri, Dr. C. D. McMillen, Prof. J. W. Kolis  
Department of Chemistry and Center for Optical Materials Science and  
Engineering Technologies (COMSET), Clemson University,  
Clemson, SC 29634-0973, USA

[b] Dr. T. M. Smith Pellizzeri  
Department of Chemistry and Biochemistry, Eastern Illinois University,  
Charleston, IL 61920, USA

[c] Dr. G. Morrison, Prof. H.-C. zur Loyer  
Department of Chemistry and Biochemistry, University of South Carolina,  
Columbia, SC 29208, USA

[d] Prof. J. W. Kolis  
485 H.L. Hunter Laboratories  
Clemson, SC 29634  
E-mail: kjoseph@clemson.edu

Supporting information and ORCID(s) from the author(s) for this article are available on the WWW under <https://doi.org/10.1002/ejic.202000518>.

blocks. We targeted these building blocks as potentially interesting magnetic first-row transition metal vanadates. Specifically, we investigated the use of manganese and cobalt as these have been very good metal building blocks in the past. Here we report the initial results of this work with three new structures,  $\text{NaMn}_4(\text{VO}_4)_3$  (**1**),  $\text{Na}_2\text{Mn}_3(\text{VO}_4)_3$  (**2**), and  $\text{Na}_2\text{Co}_3(\text{VO}_4)_2(\text{OH})_2$  (**3**), each containing sodium ions as critical components of the structures. We report the details of these new structures as well as spectroscopic and magnetic properties.

## 2. Results and Discussion

### 2.1. Synthesis of $\text{NaMn}_4(\text{VO}_4)_3$ (**1**), $\text{Na}_2\text{Mn}_3(\text{VO}_4)_3$ (**2**), and $\text{Na}_2\text{Co}_3(\text{VO}_4)_2(\text{OH})_2$ (**3**)

Our investigations into the synthesis of new metal oxide materials in hydrothermal brines have stemmed partly from our interest in exploring the conditions whereby related crystals are formed in natural systems.<sup>[16]</sup> The vanadates have emerged as a favored test system because of their proclivity to form materials with interesting structural and magnetic properties. This attractive behavior is due in large part to the ability of the tetrahedral  $(\text{VO}_4)^{3-}$  to adopt a wide range of bridging modes with open-shell transition metal ions, and also to form polyvanadate building blocks leading to an almost infinite array of structural possibilities. We also find that the product profile is highly sensitive to the nature of the mineralizer brines, with one or more of the components of the brine fluid sometimes, but not always, becoming incorporated in the isolated products. This rich chemistry makes the vanadates an almost ideal testbed for the study of brine fluids on new material formation. Thus far we have investigated rubidium-, cesium-, strontium-, and barium-based halide brines with transition metal vanadates under hydrothermal conditions.<sup>[7–9,17–19,21–24]</sup> In some cases we have observed halide incorporation into the lattice, such as in  $\text{Ba}_5\text{Mn}_3(\text{V}_2\text{O}_7)_3(\text{OH},\text{Cl})\text{Cl}_3$ ,<sup>[24]</sup>  $\text{Ba}_2\text{Mn}(\text{V}_2\text{O}_7)(\text{OH})\text{Cl}$ ,<sup>[24]</sup> and  $\text{Cs}_3\text{Mn}(\text{VO}_3)_4\text{Cl}$ .<sup>[22]</sup> In other cases, however, we observe cation incorporation into the lattice but no halide, for example in  $\text{Sr}_2\text{Mn}_2(\text{V}_3\text{O}_{10})(\text{VO}_4)$ ,<sup>[23]</sup>  $\text{Cs}_6\text{Mn}(\text{H}_2\text{O})_2(\text{VO}_3)_8$ ,<sup>[21]</sup> and  $\text{Cs}_5\text{KMn}(\text{H}_2\text{O})_2(\text{VO}_3)_8$ .<sup>[21]</sup> We have not yet been able to detect any correlation as to when and how the brine components incorporate into the lattice, but we do observe that the structures produced are extremely sensitive to the stoichiometry of the starting materials as well as the nature of the brine.

The sodium compounds presented herein,  $\text{NaMn}_4(\text{VO}_4)_3$  (**1**),  $\text{Na}_2\text{Mn}_3(\text{VO}_4)_3$  (**2**), and  $\text{Na}_2\text{Co}_3(\text{VO}_4)_2(\text{OH})_2$  (**3**) were all synthesized from brine mineralizers made of a mixture of sodium hydroxide and sodium chloride. They represent the initial results of our first systematic examination of sodium ion mineralizers. This is obviously a significant step given the importance of sodium in geothermal brines, making this work of particular mineralogical relevance. The sensitivity of the chemistry to reaction conditions and the structural complexity of the products strongly suggest that these represent only the very tip of the iceberg of new sodium transition metal vanadates. The significant differences in the synthesis of the two different manganese compounds, **1** and **2**, are partly the result of Mn/V

stoichiometry of the reactions and the oxidation state of the Mn starting material in each case. For **1**, the manganese starting material used is  $\text{Mn}_2\text{O}_3$ , and the reaction involves a 2:1 molar ratio of Mn/V. For **2**, the manganese starting material is  $\text{MnO}$ , and the reaction was a 1:1 molar ratio of Mn/V. An interesting observation is that compound **1** contains only  $\text{Mn}^{2+}$  so the manganese is reduced during the reaction. In contrast, **2**, is a mixed valent Mn product (see below). Hence, the manganese is partially oxidized during the progress of the reaction. For these reactions, however, the general trends of the molar ratios of reactants are reflected in the products, with **1**, containing an excess of Mn in  $\text{NaMn}_4(\text{VO}_4)_3$  resulting from the reaction with excess manganese, while **2**,  $\text{Na}_2\text{Mn}_3(\text{VO}_4)_3$ , contains equimolar Mn and V, mirroring the stoichiometry of the starting materials. In the case of the cobalt-containing compound, **3**, the initial reactions employed mixed  $\text{Co}^{2+}/\text{Co}^{3+}$  in the starting material  $\text{Co}_3\text{O}_4$ , but produced only  $\text{Co}^{2+}$  in the product. In this case, just as for manganese in **1**, cobalt is reduced during the reaction. We do not yet fully understand why this oxidation and reduction occurs during hydrothermal reactions; however, we do observe it often. Here, the redox behavior of manganese and cobalt is clearly necessary to obtain proper charge balance, so the activity may be encouraged by the stability of these particular crystalline phases **1–3**. In the case of **3**, when the reaction was modified to only include  $\text{Co}^{2+}$  in the starting material (as  $\text{CoO}$ ), the yield and size of  $\text{Na}_2\text{Co}_3(\text{VO}_4)_2(\text{OH})_2$  crystals improved considerably. In all cases, reversing the mineralizer concentrations (to 3 M NaOH + 1 M NaCl for the manganese-based systems, and 3 M NaCl + 1 M NaOH for the cobalt-based system), did not produce the title compounds **1–3**. In the manganese-based systems,  $\text{NaMnVO}_4$  was obtained instead of **1** and **2**. In cobalt-based system, reversing the mineralizer system resulted in recrystallization of  $\text{Co}_3\text{O}_4$  instead of the formation of **3**.

### 2.2. Crystal Structures of $\text{NaMn}_4(\text{VO}_4)_3$ (**1**), $\text{Na}_2\text{Mn}_3(\text{VO}_4)_3$ (**2**), and $\text{Na}_2\text{Co}_3(\text{VO}_4)_2(\text{OH})_2$ (**3**)

Structure **1** crystallizes in the noncentrosymmetric tetragonal space group  $I-42d$ , and is built from equivalent interlocking manganese oxide chains, coordinated to one another by  $(\text{VO}_4)^{3-}$  vanadate groups to form a complex three-dimensional structure, with sodium residing in the void spaces and charge balancing the formula. The manganese chain substructures are made up of two unique manganese atoms, Mn1 and Mn2. These manganese atoms edge-share through oxygen edges to form the zig-zag spiral chains that make up the backbone of the structure. Individual manganese oxide chains then coordinate to one another through corner-sharing oxo groups (Figure 1).

One of the manganese chains propagates along the  $a$ -axis, and the other along the  $b$ -axis, perpendicular to each other, in accordance with the four-fold symmetry of the structure (Figure 2). As the perpendicular chains intersect (Figure 2), they form a three-dimensional manganese oxide framework. Both manganese atoms are octahedral and the edge-sharing interaction between Mn1 and Mn2 occurs between atoms O1 and O3. The average Mn–O bond length is 2.162 Å, within the expected

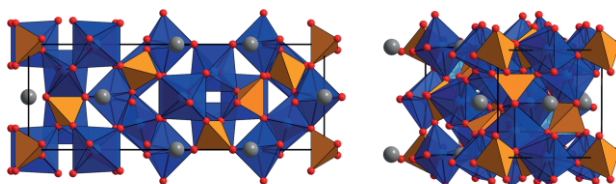


Figure 1. Unit cell view of  $\text{NaMn}_4(\text{VO}_4)_3$  (**1**) along the  $a$ -axis (left) and just off of the  $c$ -axis (right). Color scheme sodium: gray spheres, vanadium: orange polyhedra, manganese: blue octahedra, oxygen: red spheres.

range for  $\text{Mn}^{2+}$ . The Mn1 and Mn2 sites are located at 8c and 8d Wyckoff sites, respectively, but exhibit different distortions from ideal octahedral symmetry when compared to one another. The Mn1 site features a more even distribution of Mn–O bond lengths [2.156(2) Å to 2.2343(19) Å], coupled with more significant *trans*-O–Mn–O angular distortion [*cis*-O–Mn–O angles from 80.74(7)° to 105.12(8)° and *trans*-O–Mn–O angles from 156.58(11)° to 170.36(8)°], while the Mn2 site exhibits a greater degree of Mn–O bond length distortion [2.082(2) Å to 2.254(2) Å], but with more significant *cis*-O–Mn–O angular distortion [*cis*-O–Mn–O angles from 73.11(10)° to 102.56(12)° and *trans*-O–Mn–O angles from 165.16(8)° to 175.06(12)°].

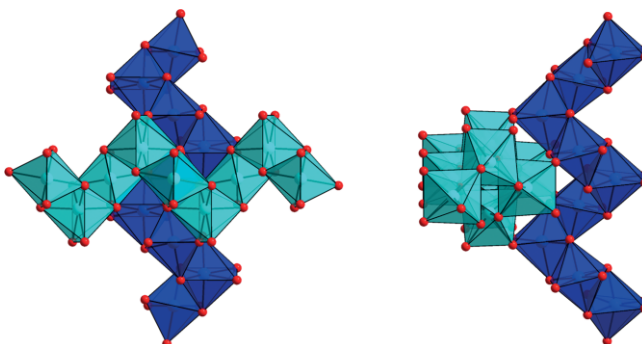


Figure 2. The intersecting chains of  $\text{NaMn}_4(\text{VO}_4)_3$  (**1**), displayed in cyan and blue to distinguish between manganese oxide chains. The chains are viewed along the  $bc$ -plane (left) and just off of the  $a$ -axis (right).

There are also two unique vanadium atoms in the structure, V1 and V2, which coordinate the manganese chains and occupy tetrahedral gaps between the interwoven chains. In this way, each vanadium atom acts as a “space filler” within the structure. The first vanadium atom, V1, is tetrahedral in geometry and coordinates to O1 and O2 along with their symmetry equivalent atoms. This connectivity provides corner-sharing interactions between V1 with Mn1 and Mn2. The second vanadium atom is also tetrahedral in geometry, coordinating to one symmetry equivalent oxygen atom, O3, which creates corner-sharing interactions with both Mn1 and Mn2. Hence, there are no terminal V–O oxo bonds in this structure, and all the V–O bond lengths occur within a relatively narrow range [1.7184(19) Å to 1.726(2) Å], averaging 1.722(2) Å, as expected for  $\text{V}^{5+}$ .

Structure **2**,  $\text{Na}_2\text{Mn}_3(\text{VO}_4)_3$ , is also composed of manganese oxide chains that form layers and are coordinated to one another through isolated  $(\text{VO}_4)^{3-}$  tetrahedra. These vanadate ions also serve to link the layers to one another via corner-sharing, forming the three-dimensional structure. The sodium atoms act

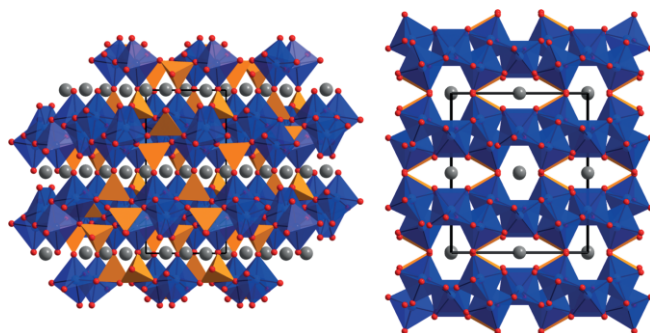


Figure 3. View of  $\text{Na}_2\text{Mn}_3(\text{VO}_4)_3$  (**2**) along the  $a$ -axis (left) and  $c$ -axis (right). Color scheme is the same as in Figure 1.

to charge-balance the compound and reside in the small cavities formed by the connectivity of the manganese vanadate layers (Figure 3).

Compound **2** contains two unique Mn sites. The Mn1 site is assigned as  $\text{Mn}^{2+}$  based on bond valence sum analysis [SI, Table S1; with average Mn–O = 2.191(2) Å], while the Mn2 site is assigned as  $\text{Mn}^{2+/3+}$  [average Mn–O = 2.093(3) Å] with mixed 2+ and 3+ oxidation states equally distributed over the equivalent site. Since Mn1 sits on the 4e Wyckoff site and Mn2 sits on the 8f Wyckoff site, this provides the necessary charge balance for the compound’s empirical formula as  $\text{Na}_2\text{Mn}_2^{2+/3+}\text{Mn}^{2+}(\text{VO}_4)_3$ . The manganese oxide chains in **2** are built from edge-sharing dimers of Mn2 octahedra through two symmetry-equivalent O4 atoms that are connected to one another by Mn1 octahedra, again via edge-sharing (of O1 and O3), to propagate a chain along the  $ac$  face diagonal (Figure 4). These chains are connected to one another in the  $ac$ -plane through the V1 tetrahedra, which connect O3 and O6 atoms of one chain to symmetry equivalent O3 and O6 atoms of a neighboring chain. This creates manganese vanadate sheets

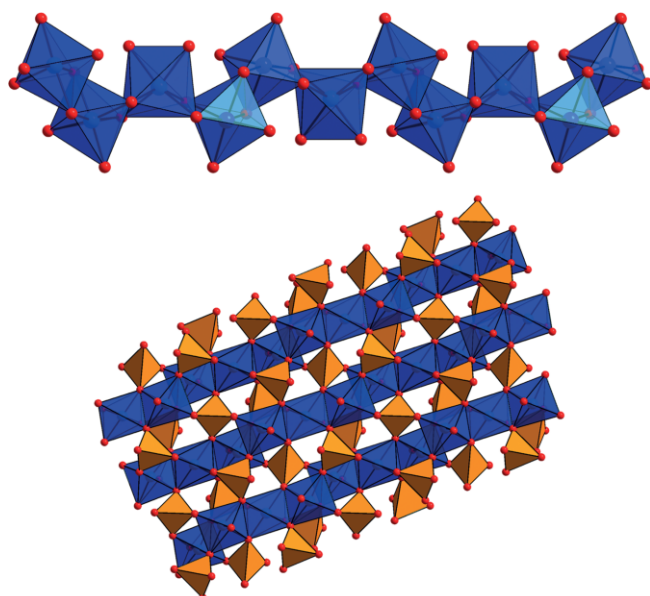


Figure 4. Manganese oxide chain propagating within the  $ac$ -plane (top), and the manganese vanadate sheet substructure viewed along the  $b$ -axis (bottom) in the structure of **2**. Color scheme is the same as in Figure 1.

normal to the *b*-axis. The V2 tetrahedra bond to the O2 and O4 atoms of one chain and the O1 atom of a neighboring chain in the sheet, but also connect neighboring sheets along the *b*-axis through the fourth V–O bond of the tetrahedron, to O5. This ultimately creates the three-dimensional manganese vanadate framework. In a similar fashion to **1**, the two unique Mn sites of **2** exhibit different degrees of bond length distortions and significant angular distortions from ideal octahedra. The Mn1 site possesses a fairly narrow distribution of Mn–O bond lengths [2.176(2) Å to 2.204(2) Å] while the Mn2 site has a wider range [2.030(2) Å to 2.190(2) Å]. Both sites exhibit both *cis*- and *trans*-O–Mn–O angular distortion [for Mn1, *cis*-O–Mn–O ranges from 75.23(8)° to 111.38(9)° and *trans*-O–Mn–O ranges from 145.92(13)° to 162.73(9)°; for Mn2, *cis*-O–Mn–O ranges from 79.72(9)° to 106.12(10)° and *trans*-O–Mn–O ranges from 161.50(9)° to 174.48(9)°].

Structure **3**,  $\text{Na}_2\text{Co}_3(\text{VO}_4)_2(\text{OH})_2$ , is built from two-dimensional cobalt vanadate layers separated by layers of sodium atoms. There are two unique cobalt oxide octahedra within the structure, which oxygen-edge-share to one another, forming a layer normal to the *a*-axis, with vanadate groups decorating the top and bottom of the layers (Figure 5). Despite the lower overall symmetry of the structure, these layers have some structural similarities to Kagome nets, and this aspect is discussed more fully below. The two unique cobalt atoms are assigned as  $\text{Co}^{2+}$ , with the average Co–O bond length 2.095(2) Å, in the range expected for  $\text{Co}^{2+}$ . These six-coordinate cobalt sites exhibit much less angular distortion than the manganese sites in compounds **1** and **2**. The hydroxide groups provide appropriate charge balance and the IR spectrum of **3** has a distinct sharp band around  $3480\text{cm}^{-1}$  confirming the presence of a terminal hydroxide group in the lattice (Figure S1). The Co1 sites are distorted octahedra edge-sharing through symmetry equivalent hydroxide groups (O1), forming chains propagating along the *b*-axis. The Co2 sites connect these chains along the *c*-axis also by oxygen edge-sharing to create the sheets.

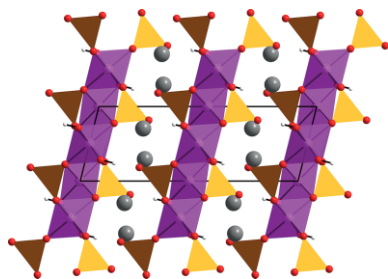


Figure 5. Unit cell depiction of  $\text{Na}_2\text{Co}_3(\text{VO}_4)_2(\text{OH})_2$  (**3**) in the *ac*-plane. Color scheme is the same as above with cobalt (purple octahedra) and hydrogen (white spheres).

Such edge shared 2-D planar systems are of interest because they often display interesting magnetic properties and thus merit a more detailed examination.<sup>[7,25–28]</sup> We recently observed a topologically similar structure in the alkali transition metal molybdate systems, where  $\text{KMn}_3(\text{MoO}_4)_2\text{O}(\text{OH})$  was found to have an ideal Kagome layer in space group  $R\bar{3}m$ .<sup>[26]</sup> Here, in the related cobalt compound, the pseudo-Kagome layers are not ideally three-fold symmetric, having Co–Co distan-

ces of 3.008(2) Å and 2.831(2) Å. The formulaic differences between the Kagome-type compound  $\text{KMn}_3(\text{MoO}_4)_2\text{O}(\text{OH})$  and  $\text{Na}_2\text{Co}_3(\text{VO}_4)_2(\text{OH})_2$  of the two studies are attributed to the valence difference of  $\text{Mo}^{6+}$  vs.  $\text{V}^{5+}$ , but the tetrahedral molybdate and vanadate oxyanions building blocks serve the same structural purpose. Despite their related topologies, the different size of the alkali metals and the need for a different number of alkali metals to charge balance the compounds thus causes different structures to be stabilized as directed by the charge of the oxyanions. There is one unique vanadium atom in the structure of **3** which sits in the spaces of the cobalt oxide layers (Figure 6), in the same way as the molybdate sits in  $\text{KMn}_3(\text{MoO}_4)_2\text{O}(\text{OH})$ . Three oxygen atoms of the vanadate tetrahedron are within the cobalt layer, while the fourth, shortest V–O bond, is terminal with respect to the cobalt vanadate layers and only interacts with sodium atoms between the layers.

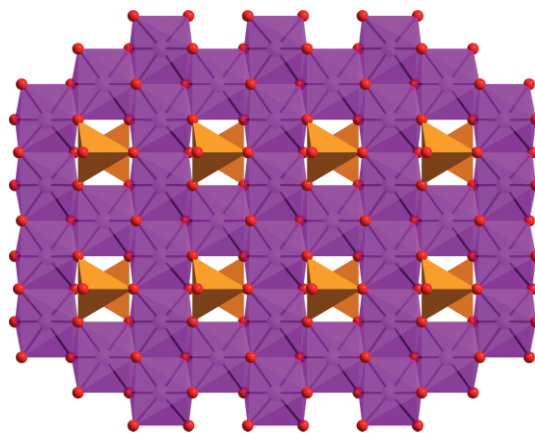


Figure 6. Cobalt vanadate layer of **3** in the *bc*-plane.

Because of its general resemblance to a Kagome layer, it is interesting to compare the cobalt vanadate layer in **3**, with that of a traditional Kagome arrangement. A great deal of insight can be gained from projecting the shared edges of the metal octahedra as simple lines and comparing the structure of **3** to a traditional Kagome layer (Figure 7). The cobalt oxide layer in **3** is comprised of a hexagonal arrangement of Co–O bonds coordinated to the four nearest hexagons on the top and bottom by a parallelogram of Co–O. An idealized Kagome layer can also be viewed as a series of edge shared delta chains<sup>[26,29,30]</sup> of metal–oxygen octahedra. This arrangement also produces hexagon shapes within the layer. Hence, despite similarities

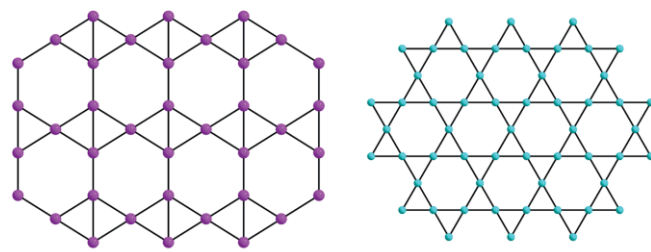


Figure 7. The cobalt oxide layer present in  $\text{Na}_2\text{Co}_3(\text{VO}_4)_2(\text{OH})_2$  with octahedral edge-sharing interactions displayed as black lines (left). A similar view of the connectivity through metal–oxide edges in an ideal Kagome net (right).

within the layer, these differences between the two-layered structures should lead to interesting but distinctly different magnetic behavior.

### 2.3. Magnetic Studies

The magnetic properties of  $\text{NaMn}_4(\text{VO}_4)_3$  (**1**) at high temperatures display paramagnetic behavior (Figure 8). Fitting the high-temperature susceptibility (100–300 K) to the Curie–Weiss law yields an effective moment,  $\mu_{\text{eff}}$ , of 5.93(3)  $\mu_{\text{B}}/\text{Mn}$ , in excellent agreement with the calculated moment of 5.92  $\mu_{\text{B}}/\text{Mn}$  for high spin  $\text{Mn}^{2+}$ , and a Weiss temperature,  $\theta_{\text{CW}}$ , of  $-183(4)$  K, indicating that antiferromagnetic interactions are dominant within the compound. A magnetic transition at  $T \approx 46$  K is characterized by a sharp increase in the susceptibility with very little splitting between the zfc and fc curves. Furthermore, the field-dependent magnetization displays a small jump at low fields followed by linear behavior up to the maximum applied field, 5 T. These data, coupled with the negative Weiss temperature, suggest that **1** is a canted antiferromagnet at low temperatures. To confirm that the observed magnetic transition is the result of an intrinsic magnetic ordering, as opposed to the presence of a small ferromagnetic/ferrimagnetic impurity, magnetic properties were measured on three separate well-formed single crys-

tals with visually clean surfaces. Shown in Figure S2, all three crystals exhibit the same magnetic behavior as the bulk sample.

The bulk magnetic properties of  $\text{Na}_2\text{Co}_3(\text{VO}_4)_2(\text{OH})_2$  (**3**) were also examined (Figure 9). The compound orders antiferromagnetically at  $T_{\text{N}} = 4.4$  K, determined from the maximum in  $\text{dM}/\text{dT}$ .<sup>[31]</sup> Fitting the high-temperature susceptibility (50–300 K) to the Curie–Weiss law yields  $\mu_{\text{eff}} = 5.05(3)$   $\mu_{\text{B}}/\text{Co}$  and  $\theta_{\text{CW}} = -26.1(5)$  K. The effective moment is higher than the calculated spin only moment of 3.87  $\mu_{\text{B}}/\text{Co}^{2+}$  but is in good agreement with the 4.1–5.2  $\mu_{\text{B}}/\text{Co}$  typically observed in high spin  $\text{Co}^{2+}$  containing compounds and is presumably a function of the well-known spin-orbit coupling effects observed in divalent cobalt ions.<sup>[32,33]</sup> The bulk magnetization as a function of field displays at least three metamagnetic transitions. Such step-wise behavior is often observed in highly anisotropic systems.<sup>[34,35]</sup> For this reason, the anisotropic magnetic properties were also measured on an oriented single crystal of **3** (Figure 9c–d). The observed magnetism indicates that the system is indeed anisotropic with the easy axis of magnetization being the crystallographic *c*-axis. The field-dependent magnetization with  $H//c$  contains two large metamagnetic transitions centered at  $H = 1.9$  and 3.4 T, whereas with  $H//b$  and  $H \perp (100)$ , smaller metamagnetic transitions are observed at  $H = 4.2$  T and  $H = 4.7$  T, respectively.

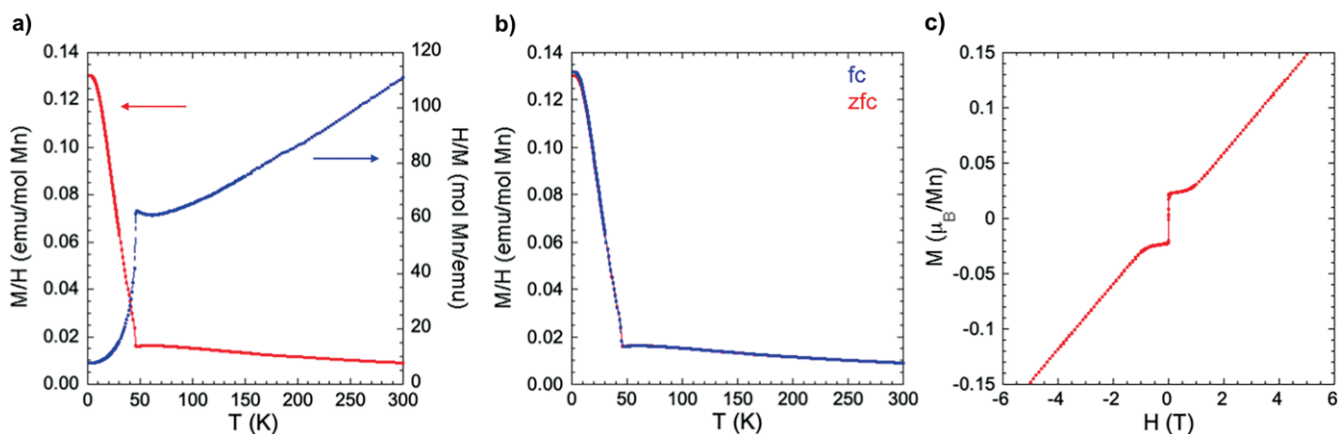


Figure 8. Magnetic properties of **1** showing (a) the zfc susceptibility and inverse susceptibility, (b) the zfc and fc susceptibilities, and (c) the magnetization as a function of field.

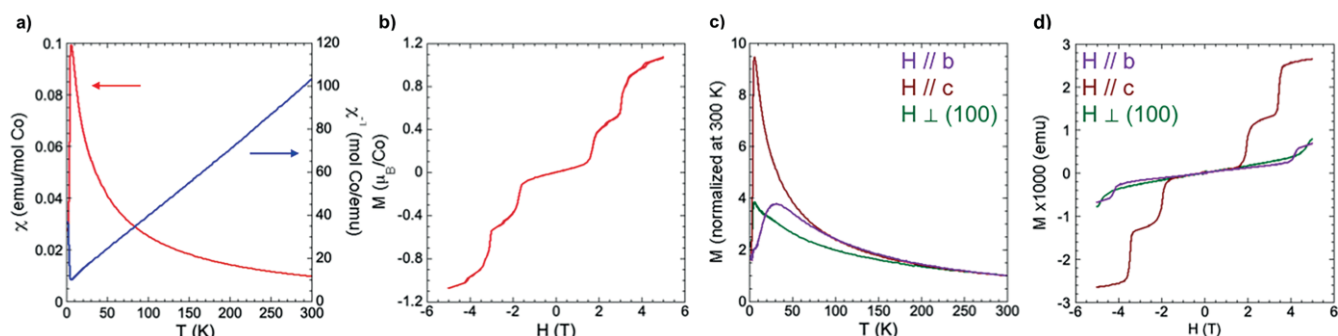


Figure 9. Magnetic properties of **3** showing (a) the zfc susceptibility and inverse susceptibility of the bulk sample, (b) the magnetization as a function of field for the bulk sample, (c) the oriented zfc susceptibility (normalized at 300 K) and (d) the oriented magnetization (shown as raw moment  $\times 1000$ ).

### 3. Conclusions

Herein we have reported on the synthesis, structural characterization, and magnetic properties of three new sodium transition metal vanadate compounds,  $\text{NaMn}_4(\text{VO}_4)_3$  (**1**),  $\text{Na}_2\text{Mn}_3(\text{VO}_4)_3$  (**2**), and  $\text{Na}_2\text{Co}_3(\text{VO}_4)_2(\text{OH})_2$  (**3**), all of which have complex structures built of edge shared metal octahedra linked in various ways by isolated vanadate groups. The compounds can all be prepared in high yields as high-quality single crystals at intermediate temperatures (580 °C) in hydrothermal fluids using concentrated brines as the mineralizer. The reactions are all highly sensitive to the nature of the brines and represent the next step in this general synthetic protocol, employing sodium brines for the first time. Compound **1** is an elegant and complex structure formed from interlocking manganese chains coordinated by vanadate to form a three-dimensional structure. Magnetic measurements suggest that it is a canted antiferromagnet with  $T_N \approx 46$  K. Compound **2** is formed from edge-sharing manganese chains that are linked by vanadate ions to form a layered structure and these layers are further connected by corner-sharing vanadates to form a three-dimensional structure. The compound contains mixed valent manganese ions with one unique site assigned as  $\text{Mn}^{2+}$  and the other site an equimolar distribution of  $\text{Mn}^{2+}$  and  $\text{Mn}^{3+}$ , which is a common structural feature of many of these types of manganese oxide chains. Structure **3** contains layers formed of edge shared distorted octahedra. The symmetry of the layers is relatively low compared to ideal Kagome lattices but there are some similar structural features and potentially interesting properties. The formula is nearly identical to a manganese molybdate made previously in similar brine conditions, which does have ideal Kagome lattice symmetry. Unlike this and other ideal Kagome layers, compound **3** displays no evidence of spin frustration but rather orders antiferromagnetically at  $T_N = 4.4$  K. It is highly anisotropic and has an easy axis of magnetization in the crystallographic *c*-direction, along with a complex range of multiple metamagnetic states as a function of magnetic field. These compounds represent the first series of products emerging from various sodium brines. The exceptional complexity of their structures, and wide range of solvent parameters available to be explored in the sodium brine fluids, strongly suggests that these samples are just the first in a large series of new materials to emerge from these unique synthetic environments.

## 4. Experimental Section

### 4.1. General Procedures

The hydrothermal reactions producing  $\text{NaMn}_4(\text{VO}_4)_3$  (**1**),  $\text{Na}_2\text{Mn}_3(\text{VO}_4)_3$  (**2**), and  $\text{Na}_2\text{Co}_3(\text{VO}_4)_2(\text{OH})_2$  (**3**) were carried out in silver tubing with a diameter of 0.25 inches and a length of 2.75 inches. The ampoules were welded shut at one end and 0.4 mL of the desired mineralizer was added to each tube followed by the addition of the solid reactants (0.27–0.16 g), and the tubes were welded shut. These tubes were then placed inside a Tuttle-seal autoclave, and the autoclave was filled with water to provide the appropriate counter pressure. The autoclaves were heated to 580 °C for 7–11 days at an average pressure of 200 MPa. After cooling the ampoules were cut open and the products were washed thoroughly

with deionized water. The chemical reactants that were used in this study were used as they were received from the supplier: NaCl (Alfa Aesar, 99 %), NaOH (Acros Organics, 98 %), CoO (Alfa Aesar, 95 %),  $\text{Co}_3\text{O}_4$  (Alfa Aesar, 99.7 %), MnO (Strem, 99 %),  $\text{Mn}_3\text{O}_4$  (Strem, 98 %), and  $\text{V}_2\text{O}_5$  (Alfa Aesar, 99.6 %).

### 4.2. Synthesis of $\text{NaMn}_4(\text{VO}_4)_3$ (**1**)

A mixture of sodium chloride (0.028 g, 0.485 mmol), manganese (II, III) oxide (0.153 g, 0.970 mmol), and  $\text{V}_2\text{O}_5$  (0.088 g, 0.485 mmol) in a 1:2:1 molar ratio were added to a silver ampule along with 0.4 mL of 3 M NaCl/1 M NaOH mineralizer, and reacted as described above. The reaction yielded dark red crystals as approximately 75 % of the product, that were identified as **1** through single-crystal X-ray diffraction, along with small black crystals of  $\text{Mn}_3\text{O}_4$ .<sup>[36,37]</sup>

### 4.3. Synthesis of $\text{Na}_2\text{Mn}_3(\text{VO}_4)_3$ (**2**)

A mixture of manganese(II) oxide (0.069 g, 0.970 mmol) and vanadium(V) oxide (0.088 g, 0.485 mmol) in a 2:1 molar ratio was added into a silver ampule along with 0.4 mL of 3 M NaCl/1 M NaOH mineralizer and reacted as described above. Black tabular crystals of **2** were isolated as the main product of the reaction (approximately 60 % of the product) along with  $\text{Mn}_3\text{O}_4$ ,<sup>[36,37]</sup> and  $\text{NaMnVO}_4$ .<sup>[38]</sup>

### 4.4. Synthesis of $\text{Na}_2\text{Co}_3(\text{VO}_4)_2(\text{OH})_2$ (**3**)

Initially, cobalt (II, III) oxide (0.082 g, 0.340 mmol) and vanadium(V) oxide (0.088 g, 0.485 mmol) in a 0.7:1 molar ratio, along with 3 M NaOH/1 M NaCl mineralizer were reacted as described above. Small dark blue tabular crystals of **3** were identified in very low yield along with black crystals of  $\text{Co}_3\text{O}_4$ .<sup>[39]</sup> However, when the reaction was changed to react cobalt(II) oxide (0.036 g, 0.485 mmol) and  $\text{V}_2\text{O}_5$  (0.088 g, 0.485 mmol) in a 1:1 ratio with 5 M NaOH as the mineralizer, large dark blue rods of **3** were isolated in higher yield, but still only comprise about 40 % of the product.

### 4.5. X-ray Diffraction

Well-formed single-crystals of  $\text{NaMn}_4(\text{VO}_4)_3$  (**1**),  $\text{Na}_2\text{Mn}_3(\text{VO}_4)_3$  (**2**), and  $\text{Na}_2\text{Co}_3(\text{VO}_4)_2(\text{OH})_2$  (**3**) were used to determine the single-crystal structures of each compound. The data were collected at room temperature using a Bruker D8 Venture Photon 100 diffractometer (Mo- $K\alpha$  radiation,  $\lambda = 0.71073$  Å) equipped with a microfocus source. The diffraction images were collected using  $\phi$  and  $\omega$ -scans. The APEX3 software suite was used for data set-up, collection, and processing.<sup>[40]</sup>

Structure solution by intrinsic phasing and structure refinement by full-matrix least square methods on  $F^2$  were used to resolve the structures. The SHELXTL software suite was used to perform structure refinements.<sup>[41]</sup> The non-hydrogen atoms were refined anisotropically in the final structural models. The hydrogen atoms of **3** were identified from the difference electron density map and their positions were refined using DFIX restraints. Table 1 provides a summary of the structural refinement data for compounds **1–3**. Table 2 provides a list of selected bond lengths and angles for the compounds of this study.

Deposition Numbers 2006444–2006446 correspond to structures **1–3** contain the supplementary crystallographic data for this paper. These data are provided free of charge by the joint Cambridge Crystallographic Data Centre and Fachinformationszentrum Karlsruhe Access Structures service [www.ccdc.cam.ac.uk/structures](http://www.ccdc.cam.ac.uk/structures).

### 4.6. Spectroscopic Characterization

Infrared (IR) spectroscopy was collected on **3** to confirm the presence of hydroxide in the crystal structure. The IR spectrum was

Table 1. Structure refinement data for  $\text{NaMn}_4(\text{VO}_4)_3$  (1),  $\text{Na}_2\text{Mn}_3(\text{VO}_4)_3$  (2), and  $\text{Na}_2\text{Co}_3(\text{VO}_4)_2(\text{OH})_2$  (3).

	$\text{NaMn}_4(\text{VO}_4)_3$ (1)	$\text{Na}_2\text{Mn}_3(\text{VO}_4)_3$ (2)	$\text{Na}_2\text{Co}_3(\text{VO}_4)_2(\text{OH})_2$ (3)
Empirical Formula	$\text{NaMn}_4\text{V}_3\text{O}_{12}$	$\text{Na}_2\text{Mn}_3\text{V}_3\text{O}_{12}$	$\text{Na}_2\text{Co}_3\text{V}_2\text{O}_{10}\text{H}_2$
F. W. (g/mol)	587.57	555.62	486.67
Temperature [K]	298	298	298
Crystal System	Tetragonal	Monoclinic	Monoclinic
Space group	$I-42d$	$C2/c$	$C2/m$
$a$ [Å]	7.0199(3)	12.0107(5)	14.5847(11)
$b$ [Å]		12.9451(5)	5.9552(4)
$c$ [Å]	19.8139(8)	6.8820(2)	5.1414(4)
$\beta$ [°]		112.0210(10)	104.068(2)
Volume [Å <sup>3</sup> ]	976.41(9)	991.95(6)	433.16(6)
Z	4	4	2
D(calcd) [mg/m <sup>3</sup> ]	3.997	3.720	3.731
Wavelength [Å]	0.71073	0.71073	0.71073
$\mu$ , mm <sup>-1</sup>	7.860	3.720	7.844
$F(000)$	1104	1048	462
Crystal Size [mm]	0.20 × 0.18 × 0.16	0.04 × 0.20 × 0.30	0.10 × 0.04 × 0.02
$\theta$ range, °	3.08 to 30.50 °	2.41 to 27.16 °	3.71 to 27.09 °
Reflections collected	4345	8527	3032
Independent Reflections	749	1101	523
Final $R$ indices	$R_1 = 0.0167^a$ , $wR_2 = 0.0360^{[b]}$	$R_1 = 0.0209^{[a]}$ , $wR_2 = 0.0683^{[b]}$	$R_1 = 0.0144^{[a]}$ , $wR_2 = 0.0422^{[b]}$
$R$ indices (all data)	$R_1 = 0.0189^{[a]}$ , $wR_2 = 0.0364^{[b]}$	$R_1 = 0.0218^{[a]}$ , $wR_2 = 0.0701^{[b]}$	$R_1 = 0.0148^{[a]}$ , $wR_2 = 0.0424^{[b]}$
Goodness-of-fit on $F^2$	1.120	1.185	1.160

[a]  $R_1 = \sum ||F_o| - |F_c|| / \sum |F_o|$ . [b]  $wR_2 = \{ \sum [w(F_o^2 - F_c^2)^2] / \sum [wF_o^2]^2 \}^{1/2}$ .

Table 2. Selected interatomic distances [Å] and angles [°] for (1), (2), and (3).

$\text{NaMn}_4(\text{VO}_4)_3$ (1)	$\text{Na}_2\text{Mn}_3(\text{VO}_4)_3$ (2)	$\text{Na}_2\text{Co}_3(\text{VO}_4)_2(\text{OH})_2$ (3)	
Mn1–O1 × 2	2.2343(19)	Mn1–O1 × 2	2.193(2)
Mn1–O2 × 2	2.156(2)	Mn1–O2 × 2	2.204(2)
Mn1–O3 × 2	2.168(2)	Mn1–O3 × 2	2.176(2)
Mn2–O1 × 2	2.1548(19)	Mn2–O1	2.084(2)
Mn2–O2 × 2	2.255(2)	Mn2–O3	2.077(2)
Mn2–O3 × 2	2.082(2)	Mn2–O4	2.106(2)
V1–O1 × 2	1.7248(19)	Mn2–O4	2.190(2)
V1–O2 × 2	1.726(2)	Mn2–O5	2.072(2)
V2–O3 × 4	1.7184(19)	Mn2–O6	2.030(2)
	V1–O3 × 2	V1–O3 × 2	1.745(2)
O2–Mn1–O2	82.27(10)	V1–O6 × 2	1.699(2)
O3–Mn1–O3	156.58(11)	V2–O1	1.730(2)
O3–Mn1–O1	83.25(7)	V2–O2	1.686(2)
O1–Mn1–O1	93.36(11)	V2–O4	1.740(2)
O1–Mn2–O2	175.06(12)	V2–O5	1.720(2)
O1–Mn2–O2	91.28(8)		O1–Co1–O2
O3–Mn2–O1	89.63(8)	O1–Mn1–O1	109.39(12)
O3–Mn2–O2	165.16(8)	O3–Mn1–O1	75.23(8)
O1–V1–O1	120.84(14)	O3–Mn1–O3	145.92(13)
O1–V1–O2	104.68(9)		O3–V1–O3
O2–V1–O2	102.11(15)	O1–Mn2–O4	91.63(9)
O3–V2–O3	105.45(6)	O3–Mn2–O4	82.62(9)
O3–V2–O3	117.84(14)	O1–Mn2–O4	161.50(9)
O3–V2–O3	117.84(14)	O6–Mn2–O4	81.69(9)

collected from single-crystal samples of (3) that were ground thoroughly with KBr to form a uniform mixture. The mixture was then pressed into a pellet, and the infrared spectrum was collected over the frequency range of 400 to 4000 cm<sup>-1</sup> at a resolution of 4 cm<sup>-1</sup> on a Nicolet Magna IR Spectrometer 550.

#### 4.7. Magnetic Studies

Magnetic properties for (1) and (3) were measured on a Quantum Design Magnetic Properties Measurement System (QD-MPMS3). For each sample, a collection of single crystals with a mass of 1–3 mg were massed on a balance sensitive to 0.01 mg and loaded un-

ground into a VSM powder holder. Temperature-dependent susceptibility data were collected under zero-field-cooled (zfc) and field-cooled (fc) conditions at an applied field of 1,000 Oe and field-dependent magnetization data were collected from -5 to 5 T at 2 K. The raw data were corrected for sample shape and radial offset effects.<sup>[42]</sup> For (1), data were also collected on three separate well-formed single crystals with visually clean surfaces. Each crystal was glued to a quartz paddle using GE 7031 Varnish. For (3), data were also collected on an oriented, plate-like single-crystal glued to a quartz paddle using GE 7031 Varnish. Data were collected for H//b, H//c, and H perpendicular to (1 0 0), corresponding to the macro-

scopic long, medium, and short axis of the crystal, respectively. Due to the comparatively small size of the crystals of **2**, it was not possible to reliably separate a suitable amount of phase pure material from the residual  $\text{NaMnVO}_4$ <sup>[38]</sup> and  $\text{Mn}_3\text{O}_4$ <sup>[36,37]</sup> products for magnetic characterization.

## Acknowledgments

We are indebted to the National Science Foundation NSF-DMR-1808371 and NSF-OIA-1655740 for financial support of the synthesis and crystal growth. For the magnetic measurements, we acknowledge NSF-OIA-1655740 and DMR-1806279.

**Keywords:** Hydrothermal · Crystal growth · Vanadates · Transition metals · Sodium vanadates · Alkali vanadates · Magnetic properties

[1] T. Chirayil, P. Y. Zavalij, M. S. Whittingham, *Chem. Mater.* **1998**, *10*, 2629–2640.

[2] J. Livage, *Materials* **2010**, *3*, 4175–4195.

[3] N. A. Chernova, M. Roppolo, A. C. Dillon, M. S. Whittingham, *J. Mater. Chem.* **2009**, *19*, 2526–2552.

[4] J. Yeon, A. S. Sefat, T. T. Tran, P. S. Halasyamani, H.-C. zur Loyer, *Inorg. Chem.* **2013**, *52*, 6179–6186.

[5] W. L. Queen, J. P. West, S.-J. Hwu, D. G. VanDerveer, M. C. Zarzyzny, R. A. Pavlick, *Angew. Chem. Int. Ed.* **2008**, *47*, 3791–3794; *Angew. Chem.* **2008**, *120*, 3851.

[6] Y. Oka, T. Yao, N. Yamamoto, *J. Solid State Chem.* **2000**, *152*, 486–491.

[7] L. D. Sanjeewa, M. A. McGuire, C. D. McMillen, D. Willett, G. Chumanov, J. W. Kolis, *Inorg. Chem.* **2016**, *55*, 9240–9249.

[8] L. D. Sanjeewa, M. A. McGuire, C. D. McMillen, V. O. Garlea, J. W. Kolis, *Chem. Mater.* **2017**, *29*, 1404–1412.

[9] L. D. Sanjeewa, M. A. McGuire, V. O. Garlea, L. Hu, G. Chumanov, C. D. McMillen, J. W. Kolis, *Inorg. Chem.* **2015**, *54*, 7014–7020.

[10] T. Suzuki, M. Katsumura, K. Taniguchi, T. Arima, T. Katsufuji, *Phys. Rev. Lett.* **2007**, *98*, 127203.

[11] D. Dai, M.-H. Whangbo, *J. Chem. Phys.* **2004**, *121*, 672–680.

[12] H. Ben Yahia, E. Gaudin, J. Darriet, M. Banks, R. K. Kremer, A. Villesuzanne, M.-H. Whangbo, *Inorg. Chem.* **2005**, *44*, 3087–3093.

[13] S.-J. Hwu, M. Ulutagay-Kartin, J. A. Clayhold, R. Mackay, T. A. Wardojo, C. J. O'Connor, M. Krawiec, *J. Am. Chem. Soc.* **2002**, *124*, 12404–12405.

[14] W. L. Queen, J. P. West, J. Hudson, S.-J. Hwu, *Inorg. Chem.* **2011**, *50*, 11064–11068.

[15] D. E. Bugaris, H.-C. zur Loyer, *Angew. Chem. Int. Ed.* **2012**, *51*, 3780–3811; *Angew. Chem.* **2012**, *124*, 3844.

[16] C. D. McMillen, J. W. Kolis, *Dalton Trans.* **2016**, *45*, 2772–2784.

[17] L. D. Sanjeewa, M. A. McGuire, T. M. Smith Pellizzeri, C. D. McMillen, V. Ovidiu Garlea, D. Willett, G. Chumanov, J. W. Kolis, *J. Solid State Chem.* **2016**, *241*, 30–37.

[18] L. D. Sanjeewa, C. D. McMillen, D. Willett, G. Chumanov, J. W. Kolis, *J. Solid State Chem.* **2016**, *236*, 61–68.

[19] L. D. Sanjeewa, C. D. McMillen, M. A. McGuire, J. W. Kolis, *Inorg. Chem.* **2016**, *55*, 12512–12515.

[20] T. M. Smith Pellizzeri, C. D. McMillen, Y. Wen, G. Chumanov, J. W. Kolis, *Eur. J. Inorg. Chem.* **2019**, *2019*, 4538–4545.

[21] T. M. S. Pellizzeri, C. D. McMillen, K. Ivey, J. W. Kolis, *J. Chem. Crystallogr.* **2019**, DOI <https://doi.org/10.1007/s10870-019-00787-4>.

[22] T. M. S. Pellizzeri, M. A. McGuire, C. D. McMillen, Y. Wen, G. Chumanov, J. W. Kolis, *Dalton Trans.* **2018**, *47*, 2619–2627.

[23] T. M. Smith Pellizzeri, C. D. McMillen, S. Pellizzeri, Y. Wen, R. B. Getman, G. Chumanov, J. W. Kolis, *J. Solid State Chem.* **2017**, *255*, 225–233.

[24] T. M. Smith Pellizzeri, C. D. McMillen, Y. Wen, G. Chumanov, J. W. Kolis, *Inorg. Chem.* **2017**, *56*, 4206–4216.

[25] T. M. S. Pellizzeri, L. D. Sanjeewa, S. Pellizzeri, C. D. McMillen, V. Ovidiu Garlea, F. Ye, A. S. Sefat, J. W. Kolis, *Dalton Trans.* **2020**, *49*, 4323–4335.

[26] T. M. Smith Pellizzeri, C. D. McMillen, J. W. Kolis, *Chem. Eur. J.* **2020**, *26*, 597–600.

[27] O. V. Yakubovich, E. V. Yakovleva, A. N. Golovanov, A. S. Volkov, O. S. Volkova, E. A. Zvereva, O. V. Dimitrova, A. N. Vasiliev, *Inorg. Chem.* **2013**, *52*, 1538–1543.

[28] Y. Qi, T. Brintlinger, J. Cumings, *Phys. Rev. B* **2008**, *77*, 094418.

[29] H. Kikuchi, Y. Fujii, D. Takahashi, M. Azuma, Y. Shimakawa, T. Taniguchi, A. Matsuo, K. Kindo, *J. Phys. Conf. Ser.* **2011**, *320*, 012045.

[30] R.-X. Yao, Y.-L. Qin, F. Ji, Y.-F. Zhao, X.-M. Zhang, *Dalton Trans.* **2013**, *42*, 6611–6618.

[31] M. E. Fisher, *Philos. Mag. J. Theor. Exp. Appl. Phys.* **1962**, *7*, 1731–1743.

[32] F. A. Cotton, G. Wilkinson, *Advanced Inorganic Chemistry: A Comprehensive Text*, Interscience Publishers, **1962**.

[33] K. A. Ross, J. M. Brown, R. J. Cava, J. W. Krizan, S. E. Nagler, J. A. Rodriguez-Rivera, M. B. Stone, *Phys. Rev. B* **2017**, *95*, 144414.

[34] E. Morosan, S. L. Bud'ko, P. C. Canfield, M. S. Torikachvili, A. H. Lacerda, *J. Magn. Magn. Mater.* **2004**, *277*, 298–321.

[35] G. Morrison, J. Prestigiacomo, N. Haldolaarachchige, B. K. Rai, D. P. Young, S. Stadler, E. Morosan, J. Y. Chan, *J. Solid State Chem.* **2016**, *236*, 186–194.

[36] B. Boucher, R. Buhl, M. Perrin, *J. Phys. Chem. Solids* **1971**, *32*, 2429–2437.

[37] K. Dwight, N. Menyuk, *Phys. Rev.* **1960**, *119*, 1470–1479.

[38] H. Ben Yahia, E. Gaudin, K. Boulahya, J. Darriet, W.-J. Son, M.-H. Whangbo, *Inorg. Chem.* **2010**, *49*, 8578–8582.

[39] J. P. Picard, G. Baud, J. P. Besse, R. Chevalier, *J. Common Met.* **1980**, *75*, 99–104.

[40] APEX 3, Bruker-AXS Inc., Madison, WI, **2015**.

[41] G. M. Sheldrick, *Acta Crystallogr. Sect. A* **2008**, *64*, 112–122.

[42] G. Morrison, H.-C. zur Loyer, *J. Solid State Chem.* **2015**, *221*, 334–337.

Received: May 28, 2020